LANGMUIR

pubs.acs.org/Langmuir Article

Modulation of Oil/Polymer Nanocapsule Size via Phase Diagram-Guided Microfluidic Coprecipitation

Joseph Rosenfeld, Francois Ganachaud, and Daeyeon Lee*



Cite This: Langmuir 2023, 39, 5477-5485



Read Online

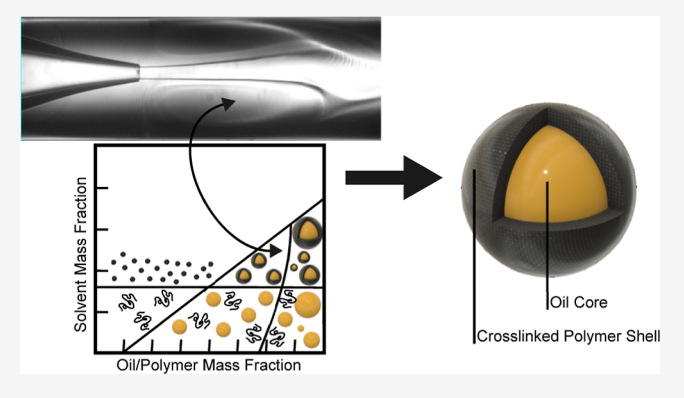
ACCESS

III Metrics & More

Article Recommendations

Supporting Information

ABSTRACT: Flow-based nanoprecipitation of different solutes via rapid mixing of two miscible liquids is a scalable strategy for manufacturing nanoparticles with various shapes and morphologies. Controlling the size of nanoparticles in flow-based nanoprecipitation, however, is often left to empirical variations in the flow rate ratios or the total flow rate of the two streams. In this work, we investigate the coprecipitations of oil and polymer to form nanocapsules via the Ouzo effect using glass capillary microfluidics across a range of mixing conditions. In the range of flow rates studied, the two streams mix convectively in microvortices formed at the junction of the two stream inlets. Using computational fluid dynamics simulations and glass capillary microfluidic nanoprecipitation, we establish a relationship between



the precipitation conditions occurring experimentally in situ and the location on the ternary Ouzo phase diagram where precipitation is taking place. We find that a key variable in the resulting average diameter of the fabricated capsules is the degree of supersaturation experienced by both the oil and the polymer in the vortex zone of the device, showing a strong correlation between the two values. The control over the nanocapsule size by varying the extent of supersaturation of both precipitants is demonstrated by using two oils having distinct phase diagrams. This work provides a systematic approach to controlling the size of nanoparticles fabricated via continuous nanoprecipitation by linking the in situ flow conditions to ternary phase diagram behavior, enabling accurate control over nanocapsule size.

■ INTRODUCTION

Nanocapsules with a hydrophobic core surrounded by a cross-linked hydrophilic shell have a number of useful applications in various fields, including drug delivery, cosmetics, and food science. The hydrophobic core of the nanocapsule can be used to encapsulate a drug or an active ingredient, protecting it from degradation and allowing it to be released in a controlled manner. The hydrophilic shell of the nanocapsule enables stable dispersion of the hydrophobic material in aqueous media and thus allows various hydrophobic actives to be easily incorporated into final products such as creams and food products. The shell thickness can also be changed to control the release kinetics of the encapsulated species.

Among different methods of producing nanocapsules, nanoprecipitation has recently emerged as a versatile technique to fabricate nanocapsules made of various components. At the core of nanoprecipitation lies a hydrophobic solute dissolved in a polar organic solvent which is mixed with a nonsolvent of the solute (typically water). The related ternary phase diagram consists of a one-phase region where the existence of surfactant-free thermodynamically stable microemulsions has been reported, a two-phase region where rapid precipitation and demixing of the hydrophobic species occurs by spinodal decomposition, and a metastable nano-

precipitation region known as the Ouzo domain. 10,11 Mixing of the solute solution with the non-solvent while maintaining concentrations bounded by the Ouzo domain induces nucleation of the solute into nanometric droplets that are aggregated. These droplets coarsen with time and can settle into a metastable emulsion state having diameters of $\sim 1~\mu m$ or less depending on the preparation details. 9,11

Nanoprecipitation has been extended to co-precipitate an oily solute and a polymer such that core—shell nanocapsules form upon cross-linking of the polymer shell. ^{5,12} The technique relies on the alignment of the oil Ouzo ternary phase diagram and the cloud point of a cross-linkable polymer to ensure oil and polymer concomitant co-precipitations. ⁶ Inclusion of a cross-linker of the polymer induces subsequent shell solidification, even after solvent removal. A variety of oils

Received: January 18, 2023 Revised: March 20, 2023 Published: April 4, 2023





and polymers have been used to fabricate core—shell nanocapsules with this method. 5-8

Nanoprecipitation is commonly carried out using batch methods since small batches allow for rapid mixing of the solvent and nonsolvent, a known requirement for the production of uniform particles; 14 however, reproducibility can suffer between batches according to the extent of mixing, and scaling up while maintaining consistent product quality attributes is also challenging. 15,16 It is thus imperative to develop a continuous method of achieving nanoprecipitation in which mixing can be performed rapidly while facilitating scaleup. Microfluidics is a technique that permits precise control of flow patterns and has recently been shown to enable industrialscale production of emulsions via parallelization. 17-20 A microfluidic device designed to favor rapid mixing of two streams is a potentially powerful platform to allow translation of the nanoprecipitation technique from a batch to a continuous process. While microfluidic-based nanoprecipitation to produce nanoparticles of various molecular architectures has been dealt with, 21-23 few studies have reported on microfluidic co-precipitation of core and shell materials for the continuous production of nanocapsules. Those that do²⁴ take an empirical approach to nanoparticle/nanocapsule fabrication in terms of precursor concentrations, rather than quantitatively relying on ternary phase diagrams eliminating the guesswork in approaching the Ouzo phenomenon.^{9,10} Additionally, often polymers soluble in organic solvents are precipitated 12,24 so that use of water-soluble polymers would expand the palate and enhance the stability of nanocapsules in water-based dispersions.

In this work, the relationship between oil and polymer supersaturations and nanocapsule diameter is quantified via experimental and computational efforts, linking the Ouzo phase diagram to in situ flow conditions. The phase diagram allows one to quantify the location of efficient precipitation and the degree of supersaturation of the hydrophobic species and polymer, which are key parameters in the early-stage kinetics of the precipitation process. 14,21,22,25 We report on a system of microfluidic co-precipitation of an oil core/polymer shell capsule using glass capillary microfluidics. The core material, a biocompatible triglyceride mixture, Miglyol, is precipitated from an acetone solution according to its ternary Ouzo phase diagram, while the polymer shell, made of dextran, is precipitated by harnessing the poor solvent quality relative to the polymer of the oil precipitation conditions. Coaxial glass capillary microfluidics^{26,27} is used because of its high solvent compatibility. A tapered inner capillary with a desired diameter is nested inside a larger capillary, forming two coaxial channels through which miscible fluids can flow and mix. A range of mixing conditions are achieved by varying the inner capillary taper diameter and the total mass flow rate while keeping the acetone-water mass flow rate ratio constant. Micro-vortices are formed under the given flow conditions that enhance mixing of the two streams. Computational fluid dynamics (CFD) simulations are used to calculate the acetone and oil concentrations in the device to understand the precipitation conditions. We demonstrate that the capsule diameter can be controlled between 100 and 280 nm by using ternary phase diagrams and linking them to experimental conditions through CFD simulations. Our results indicate that nanocapsule formation and stabilization are driven by oil and polymer local supersaturations that control the early-stage kinetics of nucleation and growth and polymer precipitation. This work

provides insights into continuous coprecipitation for nanocapsule fabrication by harnessing phase diagrams to inform oil and polymer supersaturations and thus coprecipitation conditions.

■ EXPERIMENTAL SECTION

Materials. The following chemicals are purchased from Sigma-Aldrich and used as received: acetone (ACS reagent, ≥99.5%), dextran from *Leuconostoc mesenteroides* (avg. mol wt 35k–45k), hexadecane (99%), and isophorone diisocyanate (IPDI) (98%, mixture of isomers). IPDI is sensitive to humidity and is thus replaced on a regular basis (~months). Deionized water (Barnstead Nanopure, 18.2 MΩ cm) is used for the aqueous phase. Miglyol 812 N is graciously provided by IOI Oleo GmbH (Hamburg, Germany). Glass capillaries are purchased from World Precision Instruments; the outer capillary has dimensions of 2.0 mm OD/1.12 mm ID, whereas the inner capillary has dimensions of 1.0 mm OD/0.58 mm ID.

Microfluidic Device Fabrication. Microfluidic devices are fabricated using the methods described in prior publications. 26,28 Briefly, a glass capillary of dimensions 1.0 mm OD/0.58 mm ID is heated and pulled using a Sutter Instruments Flaming/Brown Micropipette Puller P-100 forming a nozzle of $\sim 1~\mu m$ diameter with the taper angle near the opening of $\sim 5^{\circ}$. The opening is widened via sandpaper to either $40/60/80/100 \pm 5~\mu m$ as measured via the internal scalebar of Micro ForgeM-380 (Narishige, Japan). This capillary is inserted into a larger capillary of dimensions 2.0 mm OD/1.12 mm ID creating inner and outer inlets, and the capillaries are coaxially aligned due to the narrow gap between the two capillaries. The device inlets are sealed off with McMaster-Carr probe needles and 5 min epoxy (Devcon). A typical device is shown in Figure S1. Connections are made to syringes via polyethylene tubing (Scientific Commodities Inc.).

Microfluidic Production of Nanocapsules. Using a microfluidic device having a specified inner capillary taper diameter described above, a syringe containing a mixture of acetone, Miglyol, and IPDI is connected to the inner capillary inlet, while a syringe containing the dextran solution is connected to the outer capillary inlet. The starting concentrations of Miglyol/IPDI in acetone are 8 × $10^{-4}/2 \times 10^{-4}$ by the mass fraction, respectively, while the dextran concentration in water is 0.1 wt %. The target final acetone mass fraction is 0.59,5 achieved by setting the mass flow rate ratio of acetone relative to the total mass flow rate to 0.59, yielding final mass fractions of Miglyol/IPDI/dextran of $4.7 \times 10^{-4}/1.2 \times 10^{-4}/4.1 \times 10^{-4}$ 10⁻⁴, respectively. Fluid flow rates are controlled via syringe pumps (Harvard Apparatus). For hexadecane capsules, the starting mass fraction in acetone is 1×10^{-3} , while the dextran concentration is held constant, and the final acetone mass fraction is set to 0.67 via the flow ratio. Empirically, flowing the fluid with the higher flow rate through the inner capillary results in larger vortices associated with enhanced mixing between the streams; thus, the fluid with the higher flow rate should be the one to flow through the inner capillary to achieve vortex mixing. In the case of mixing fluids having a high viscosity ratio, there is, however, a practical issue; if the higher-viscosity fluid flows through the inner capillary, the pressure drop required to flow the fluid increases dramatically. Common syringe pumps may not be able to produce sufficiently high pressure to drive the fluid at such high flow rates. If a solution with a viscosity that is significantly greater than that of water needs to be used, a device design that enables thorough and rapid mixing between high-viscosity-ratio fluids²⁹ may be better suited to enable nanoprecipitation.

Dynamic Light Scattering. Between 30 and 60 min following sample collection, size analysis is conducted via dynamic light scattering (DLS) (Beckman Coulter Delsa Nano C). The CONTIN method is used to analyze the scattering pattern. The viscosity and refractive index of the suspension are programed into the software to adjust for the water—acetone mixture values of 1.039 and 1.3623 cP, respectively (acetone mass fraction of 0.59). The DLS error bars are the standard deviations reported by the software analysis (CONTIN).

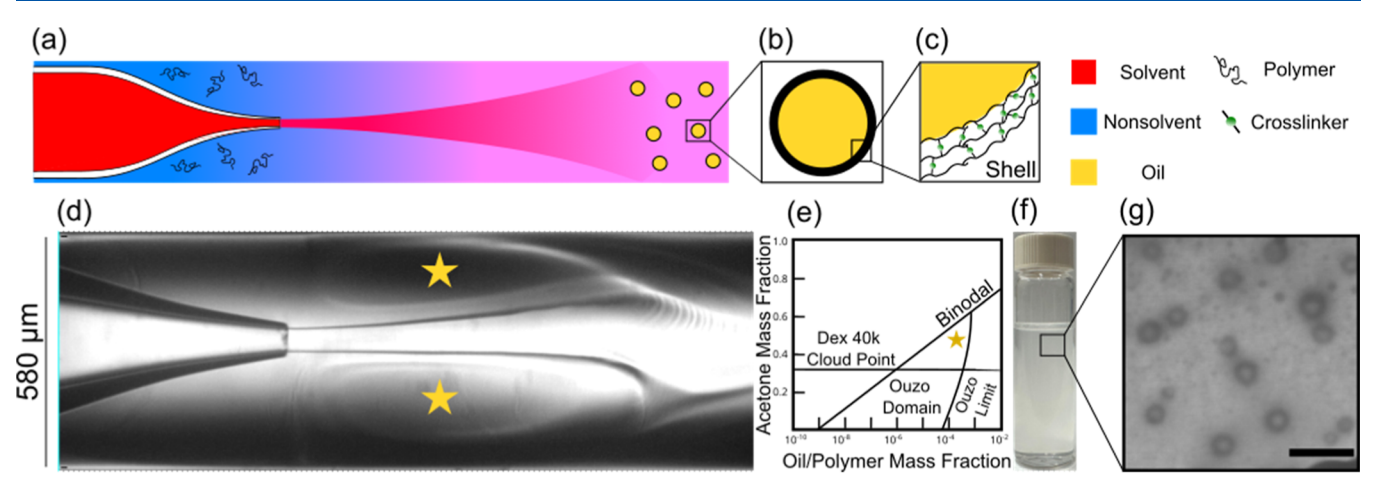


Figure 1. The top row schematically illustrates the co-precipitation process in glass capillary microfluidics, with (a) coaxial geometry and mixing zone, (b) nanocapsule downstream of the mixing zone, and (c) cross-linked polymer shell. The bottom row shows images of (d) the microfluidic device and the vortices that form alongside the junction with a star marking the vortex center; (e) a generic ternary Ouzo diagram alongside a horizontal polymer cloud point showing the opportunity window of capsule formation via coprecipitation, with a star corresponding to the in situ conditions of (d); (f) a vial with the collected sample; and (g) a representative STEM image of the nanocapsules (scale bar = 500 nm).

Scanning Transmission Electron Microscopy Imaging and Image Analysis. Scanning transmission electron microscopy (STEM) imaging is conducted using a JEOL JSM-7500F field-emission scanning electron microscope operated in transmission mode (TED), at an accelerating voltage of 15 kV and an emission current of 20 μ A. To prepare samples for imaging, an additional amount of the cross-linker is added to enhance the capsule stability. One hour after sample collection, a solution of 2 × 10⁻³ IPDI mass fraction in acetone is added in a ratio of 1:4 by mass of the IPDI solution/nanocapsule suspension, followed by mixing for 30 min. The suspension is left at room temperature for 1–2 days followed by drying out a small amount of the sample on a holey carbon grid (SPI Supplies, 200 mesh copper). Analysis of the obtained micrographs is conducted using ImageJ. Size distributions are based on 400–500 capsules per condition.

CFD Simulations. To assess the mixing conditions of the two streams under different geometries and flow rates, COMSOL Multiphysics is used to simulate the microfluidic platform environment. For computational simplicity, the microfluidic device is represented in two dimensions and is assumed to be radially symmetric about its centerline. Also, both streams are assumed to have the physical properties of water. To model the mixing of two streams, the transport of diluted species module is used to simulate a generic solute originating in the inner capillary stream at a concentration of 1 mM, while the outer capillary stream is pure water. The solute is intended to mark this stream as the acetonic stream. Its transport follows species mass transport, given by the equations

$$\nabla \cdot \mathbf{J} + \mathbf{u} \cdot \nabla c = 0 \tag{1}$$

$$\mathbf{J} = -D\nabla c \tag{2}$$

where **J** represents the species flux vector, **u** is the fluid velocity vector, **c** is the species concentration, and D is the species diffusion coefficient. The diffusion coefficient of the solute is assumed to be that of a typical small molecule, $\sim 10^{-9}$ m²/s. The velocity vector of the species is taken from the velocity field of the fluids. No flux is assumed at the capillary walls. For the flow field, the single-phase laminar flow module is used. The following differential momentum balance and continuity equations are solved for steady-state or time-invariance solutions

$$\rho(\mathbf{u} \cdot \nabla)\mathbf{u} = \nabla \cdot [-p\mathbf{I} + \mu(\nabla \mathbf{u} + (\nabla \mathbf{u})^T)]$$
(3)

$$\rho \nabla \cdot \mathbf{u} = 0 \tag{4}$$

where ρ is the fluid density, p is the fluid pressure, **I** is the identity tensor, and μ is the fluid dynamic viscosity. No slip is assumed at the capillary walls. The built-in coarse mesh size is used.

All conditions simulated yield vortices spanning in length from a few millimeters to tens of millimeters. The resulting acetone concentrations, as simulated by the diluted species, within the device are inferred across the radial dimension of the channel where the center of the vortex is found. Since the properties of water are assumed for the acetone stream, the resulting diluted species concentrations present the volume fraction of the acetone stream. To convert to mass fractions by correcting for the density difference between acetone and the water—acetone mixture, the following equation is used

$$\omega = \nu (\rho_{\text{acetone}} / \rho_{\text{total}}) \tag{5}$$

where ω and ν are the mass fraction and volume fraction of acetone, respectively, and ρ is the density of either acetone or the wateracetone mixture. The oil mass fraction at any point can then be calculated by assuming that the mixing is entirely convective ($Pe \le 4$ \times 10³); thus, the oil mass fraction is the product of the initial oil mass fraction and the local acetone mass fraction. The polymer mass fraction throughout the device can be calculated similarly. The resulting oil mass fractions and corresponding acetone mass fractions can be plotted on the ternary Ouzo diagram, and the local degree of supersaturation, S, can be determined, where S is defined as the ratio of the local oil concentration and the binodal oil concentration at the same acetone mass fraction. Since for the polymer used in this study, the cloud point occurs at a constant acetone mass fraction irrespective of the polymer mass fraction,⁵ the polymer's degree of supersaturation can be calculated as the ratio of the local acetone mass fraction to the acetone mass fraction at the cloud point.

■ RESULTS AND DISCUSSION

The glass capillary device used for nanocapsule generation and the mixing zone within such a device are schematically illustrated in Figure 1. While there are numerous geometries to choose from to efficiently mix miscible fluids, the co-axial glass capillary geometry is used in this study thanks to its ease of fabrication and relatively simple geometry allowing for efficient translation to CFD simulations to enable access to experimentally difficult to measure variables. For this microfluidic platform, the three different mixing regimes between streams have been previously identified: laminar regime—mixing between streams is largely diffusive, micro-vortex

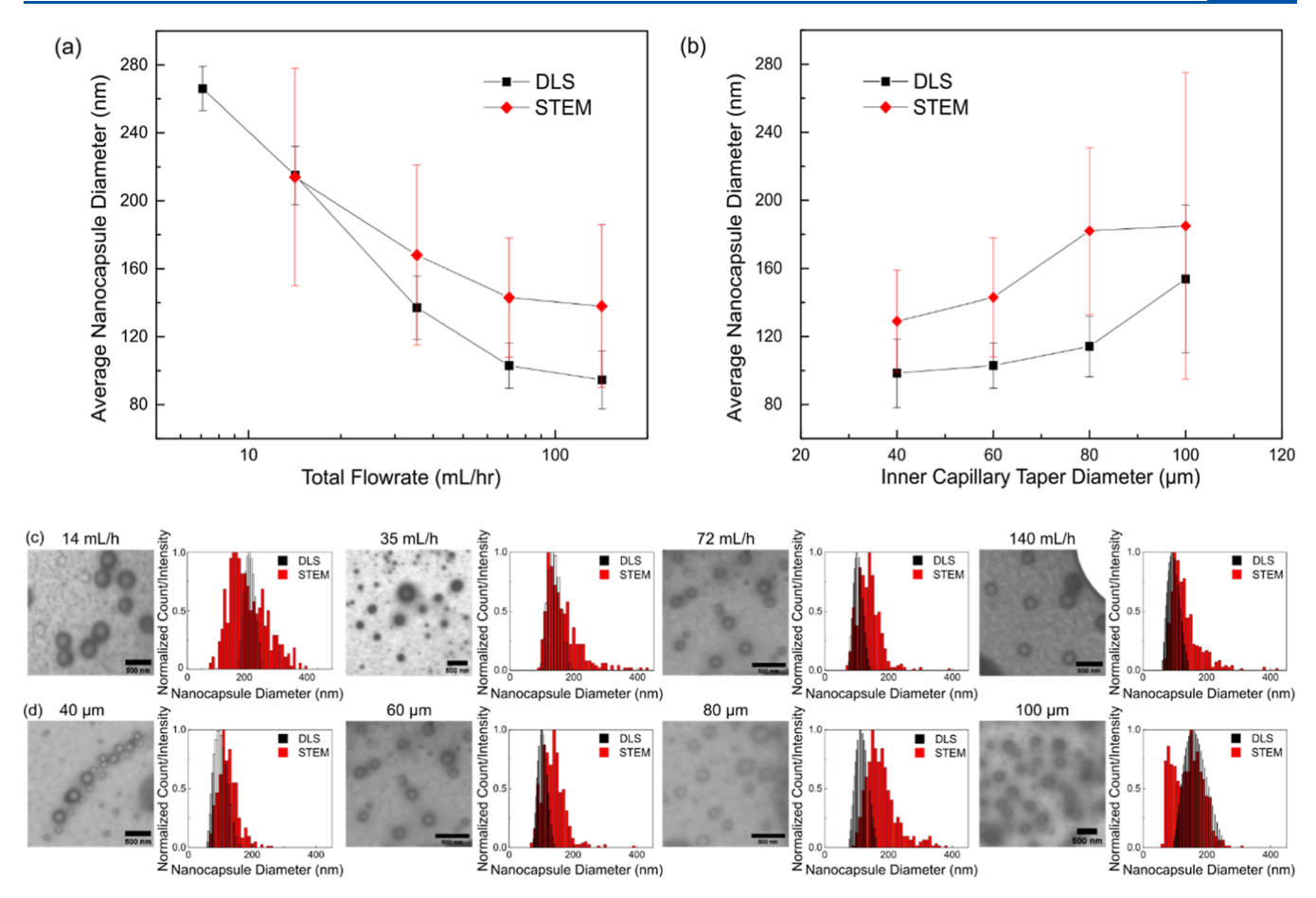


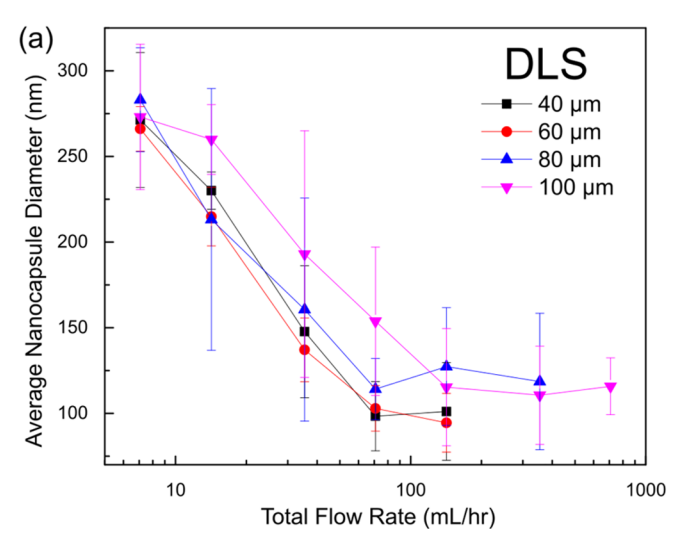
Figure 2. Effect of the total flow rate and inner capillary taper diameter on the average nanocapsule size. (a) Average capsule diameters plotted against the total volumetric flow rate, keeping the inner capillary diameter fixed at 60 μ m. The acetone/water stream volumetric flow rate ratio is constant at 1.81, for a final acetone mass fraction of 0.59. Both DLS and STEM size measurements are plotted. The DLS error bars are the standard deviations reported by the software analysis (CONTIN). The STEM error bars are the standard deviations found from measuring diameters from STEM micrographs (~400 objects per image). (b) Capsule diameters plotted as a function of the inner capillary taper diameter while the total flow rate is held constant at 70.8 mL/h. The error bars are derived in the same way as in (a). (c) Representative STEM micrographs alongside histograms and DLS intensity measurements for the conditions of (a). (d) Representative STEM micrographs alongside histograms and DLS intensity measurements for the conditions of (b). Scale bars for (c,d) are 500 nm.

regime—unsteady vortices form and mix the streams convectively, and turbulent jet regime—turbulent vortices mix the two streams. The transition between the different regimes is given in terms of the volumetric flow rate ratio of the inner capillary stream to the outer one and the local Reynolds number at the inner capillary exit. In this work, the flow rate ratio is set to \sim 2, and the local Reynolds number ranges between \sim 25 and \sim 3100; thus, the system works within the micro-vortex and turbulent jet regimes.

For the acetone/water/Miglyol ternary system,⁵ the desired acetone and oil mass fractions are set in the Ouzo domain; induction of precipitation and the specifics of the precipitation conditions rely on the exact location entered within the phase diagram. The position within the phase diagram and thus the degrees of supersaturation of both the oil and polymer are modulated in this study by the total mass flow rate, while keeping the stream flow rate ratio constant, and the inner capillary taper diameter, which controls the nozzle velocity. We hypothesize that both variables influence the vortices formed and thus the precipitation conditions. In this work, Miglyol droplets generated by the Ouzo effect are stabilized by coprecipitated dextran which is subsequently cross-linked via alcohol—isocyanate chemistry to form a shell as illustrated in

Figure 1c. The link between experimental conditions and phase diagram interpretation is accomplished via CFD simulations of the experimental conditions, allowing for extraction of acetone and oil concentrations across the range of conditions tested.

One approach to decrease the size of nanoparticles in a microfluidic nanoprecipitation scheme is to increase the total flow rate of the streams, keeping their ratio constant. 22,30,31 Increasing the total flow rate is thought to cause the streams to contact each other at greater velocities, thus reducing the mixing timescale and inducing faster nucleation rates and quicker kinetic arrest of the precipitated species. Figure 2a plots the resulting capsule diameters across an order of magnitude of flow rates, while the device geometry is held constant at an inner capillary taper diameter of 60 μ m. As hypothesized, the average capsule diameter decreases with the increasing flow rate from 266 nm at the lowest flow rate of 7.08 mL/h to 95 nm at the highest flow rate of 142 mL/h (based on DLS). The STEM histogram size distributions are wider than the DLS measurements (Figure 2c), as observed previously for nanocapsules prepared via batch nanoprecipitation.³² One possible reason for this is that DLS measurements are carried out in acetone/water mixtures in which the polymer is totally



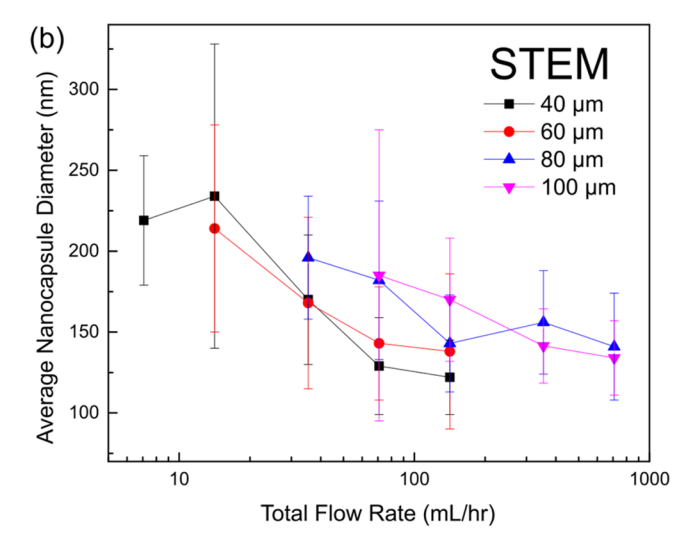


Figure 3. Variation of the total flow rate and inner capillary taper diameter across a wider range of flow rates and device geometries and the resulting average capsule diameter. (a) Average capsule diameters and standard deviations (error bars) as given by DLS. (b) Average capsule diameters and standard deviations as given by analyzing STEM micrographs (~400 objects per image).

precipitated, and thus, the shell is highly collapsed. In STEM, the sample is deposited onto a carbon film and allowed to dry out. During this process, the acetone evaporates much faster than the water, and while suspended in only water, the shell expands because of the good solvent quality. The capsule shell could become kinetically trapped in this expanded state on the carbon film.

In coaxial glass capillary microfluidics, aside from adjusting stream flow rates, another variable that directly affects the fluid mechanics is the inner capillary taper diameter. For a given flow rate, having a smaller taper diameter yields a larger nozzle velocity, and thus, the fluids mix in the vortices at different rates and at differing acetone mass fractions across a range of nozzle diameters. Here, using inner capillary taper diameters from 40 to 100 μ m with a constant total flow rate of ~70 mL/ h (flow rate ratio \sim 2) changes the local Reynolds number from \sim 630 to \sim 250. We thus hypothesize that the inner capillary taper diameter can be harnessed to control nanocapsule average diameter as well. To study the effect of microfluidic device geometry on nanocapsule size, glass capillary devices with a range of inner capillary taper diameters are fabricated, with inner capillary diameters ranging from 40 to 100 μ m. Figure 2b shows how the capsule diameter changes as a function of taper diameter at fixed stream flow rates. Nanocapsule diameters are smallest at the smallest taper diameter tested, 98 nm, increasing to 154 nm at the largest taper tested (based on DLS). One could note that in Figure 2c(1),d(4), these two STEM micrographs show a bimodal distribution of size under conditions where the larger nanocapsules are formed. Most likely here, some polymer chains of lower molecular weights have not precipitated, and after drying the samples on the grid, these free chains collapse into nanoparticles that are smaller than nanocapsules and end up being included in the size distribution. The shell thickness of the nanocapsules under different conditions qualitatively does not vary because the concentration of the polymer and cross-linker is kept constant,⁵ although the STEM micrographs suggest that for smaller capsules, the shell thickness is smaller, potentially because the polymer is distributed over a larger number of growing oil droplets.

The relative stream flow rate ratio is another variable known to affect the final size of a precipitated species in that it affects the degree of supersaturation of the precipitants. ^{5,14} Here, we illustrate this variance by holding the acetone stream flow rate constant with a 60 μ m inner capillary taper diameter while varying the water flow rate. These parameters effectively vary the acetone mass fraction of the collected samples and thus generate nanocapsules under different supersaturation conditions as given by their Ouzo phase diagram. ⁵ As shown in Figure S2, when varying the acetone mass fraction from 0.59 to 0.50, the average nanocapsule diameter varies from about 100 to 140 nm. This trend is believed to be governed by the degree of polymer supersaturation, as discussed further on.

To assess the generality of the trend of decreasing average nanocapsule diameter with the increasing total flow rate and decreasing inner capillary diameter, for each microfluidic device geometry fabricated, we vary the total flow rate over at least 1 order of magnitude. The same taper range of 40–100 μ m is used, and the total flow rate tested varies from about 7 to 700 mL/h. Consistent with the results mentioned above, we observe the general trend that for a given geometry, increasing the total flow rate yields smaller sizes, and we also observe that smaller tapers tend to yield smaller capsules in particular for flow rates above 30 mL/h as shown in Figure 3a and in Table S1. Standard deviations are also smaller for the 40 and 60 μ m devices used in comparison to those for the 80 and 100 μm devices. Close to the total flow rate of 100 mL/h, the nanocapsule diameter appears to plateau. This trend can potentially be explained by a work that previously demonstrated that when the mixing timescale is less than that of polymer coalescence, the particle diameter plateaus.³³ Here too, the mixing rate may be faster than the oil coalescence timescale, leaving the final diameter to be controlled by polymer precipitation to the oil interface and its subsequent cross-linking. Overall, the polydispersity parallels the work of others in microfluidic nanoprecipitation^{21,26} and batch methods for the same system⁵ (here, $0.047 \le \text{coefficient}$ of variation < 0.49).

For qualitative and quantitative understanding of the effects that the total flow rate and inner capillary diameter have on the fluid mechanics and the acetone fraction present in the

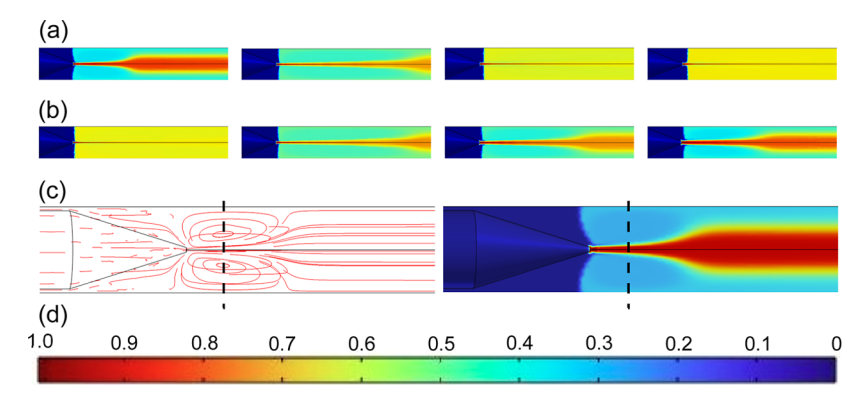


Figure 4. CFD simulations of the mixing conditions in the microfluidic environment. (a) Simulations of the experimental conditions described in Figure 2a. The inner capillary taper diameter is $60 \mu m$, and from left to right, the total flow rate is 14.2/35.4/70.8/142 mL/h while maintaining an inner to outer stream flow ratio of 1.81. (b) Simulations of the experimental conditions described in Figure 2b. The total volumetric flow rate remains constant at 70.8 mL/h, and from left to right, the inner capillary taper diameter is $40/60/80/100 \mu m$. (c) Illustration of locating the center of the vortices for quantifying the maximum degree of supersaturation that the oil experiences. The left side shows the velocity profile streamlines calculated from the simulation showing the vortex recirculation zone, and the right side shows the acetone fraction throughout the device for the same condition. The velocity profile informs the center of the vortex where the maximum degree of oil supersaturation is found. (d) Scalebar for the acetone volume fraction in the device.

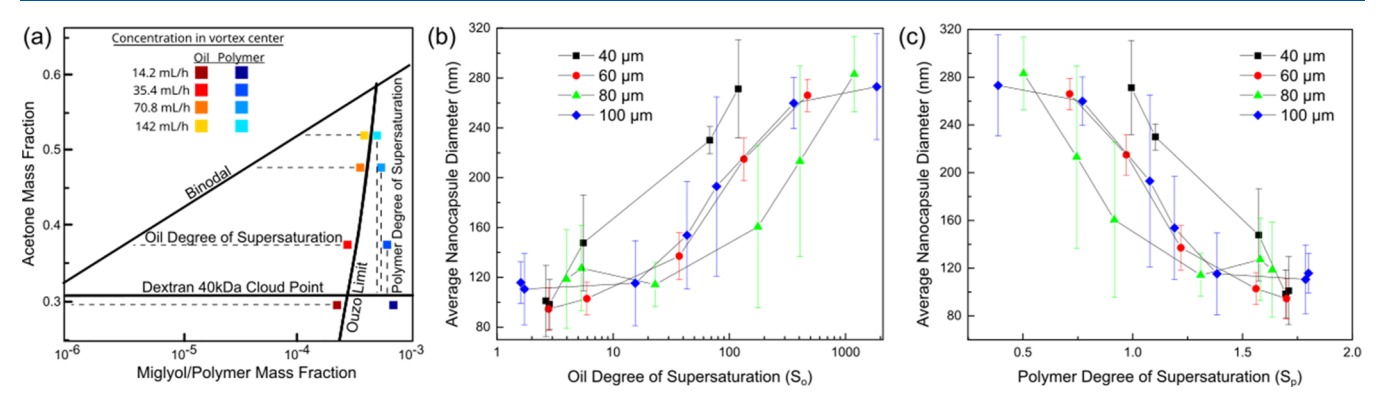
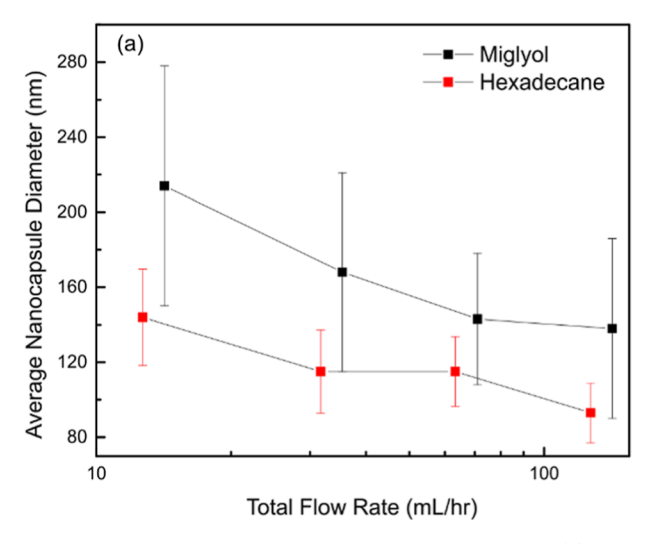


Figure 5. Phase diagram interpretation of average capsule size trends. (a) For the conditions described in Figure 2a (constant device geometry, variation of total flow rate), CFD simulations are used to simulate the mixing conditions. The acetone and oil fractions are calculated at the center of the vortex formed (Figure 4c), and the results are plotted on the ternary Ouzo phase diagram alongside the binodal, Ouzo limit, and polymer cloud point curves. The oil degree of supersaturation (distance from the binodal curve) is determined based on the smallest acetone mass fraction calculated across the center of the vortex formed. The corresponding polymer mass fraction and degree of supersaturation (distance from the cloud point curve) are plotted as well. (b) For the range of conditions tested experimentally (Figure 3), the maximum degree of oil supersaturation for each is calculated via CFD simulations, and the average capsule diameters are plotted against it. (c) Average capsule diameter plotted against the polymer degree of supersaturation for the range of conditions studied (Figure 3).

vortices, CFD simulations are undertaken. Figure 4a,b shows the simulation results for the conditions of Figure 2, showing how the acetone fraction changes as a result of flow and geometry variations, which is pivotal to quantifying the in situ oil and polymer supersaturations. Identification of the center of the vortex is important for quantifying the maximum degree of supersaturation. This can be difficult solely based on the acetone fraction profile, especially when the vortices span long lengths (>10 mm). Thus, the velocity profile streamlines are first plotted and used to clearly identify the vortex center as illustrated in Figure 4c. We observe qualitatively that relatively lower flow rates and larger inner capillary taper diameters yield smaller acetone fractions in the vortex zone of the device (which is taken to be the primary location of early-stage oil and polymer precipitation), as seen by the change in the color of the vortices. Having such information from CFD simulations allows the connection to be made between experimental conditions and the local positions on the ternary Ouzo diagram. Convective mixing between streams is guaranteed based on a high Peclet (Pe) number in the mixing zone, which

indicates that diffusive mixing is negligible relative to convective mixing ($Pe \sim 4 \times 10^3$ for the slowest flow rate used). The oil concentration in the device is given by the product of the local acetone mass fraction and the initial oil concentration in acetone, and the polymer concentration can be calculated similarly, which completes the link to the ternary diagrams.

The primary variables of interest are the degree of supersaturation that the oil and polymer experience (the ratio of the in situ oil concentration divided by the binodal oil concentration or the in situ acetone mass fraction divided by the cloud point mass fraction for polymer supersaturation) for a given set of geometry and flow conditions. Due to the convective nature of the mixing between streams in the vortex zone, the vortices have a nearly uniform concentration of the acetone and thus oil and polymer throughout their volume, and given that the onset of nanoprecipitation is rapid, the conditions experienced in the vortices are taken to be the oil precipitation conditions for a given set of experimental conditions. As a representative mapping of experimental



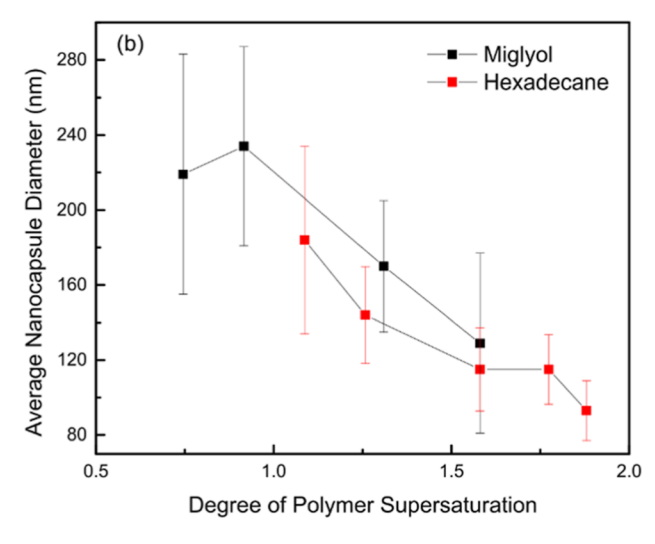


Figure 6. Comparison of hexadecane and Miglyol capsules. (a) Miglyol and hexadecane capsule diameters plotted against the total flow rate. In a similar manner to the Miglyol capsules, for hexadecane, the device geometry is held constant with a 60 μ m taper, and the total flow rate is varied across an order of magnitude of flow rates. For hexadecane, the acetone/water volumetric flow rate ratio is held constant at 2.58 for a final acetone mass fraction of 0.67. The error bars are the standard deviation from counting capsule diameters with STEM micrographs (~400 capsules per condition) (Figure S5). (b) Average nanocapsule diameter plotted against the degree of polymer supersaturation for both the Miglyol and hexadecane systems. The error bars are derived in the same way as in (a).

conditions onto the ternary phase diagram, the conditions described in Figure 2a (constant inner taper diameter of 60 μ m, variation of the total flow rate, constant flow rate ratio) are simulated and mapped onto the ternary phase diagram (Figure 5a). For flow rates below ~20 mL/h, the vortices are composed of a large fraction of water (≥ 0.7), and hence, the oil in these vortices experiences a greater degree of supersaturation. However, the polymer then experiences a small degree of supersaturation or is not supersaturated at all, directly affecting its precipitation behavior. It is known that to induce rapid nucleation rates and thus rapid cessation of the nucleation stage, a high degree of oil supersaturation is desired. 14,33 Thus, a position on the ternary diagram favoring high oil supersaturation would be desired. However, in this system, stabilization of the precipitated oil relies on the coprecipitated polymer to be deposited at the interface before further (slow) cross-linking. Conditions favoring high oil supersaturation generate low or no polymer supersaturation, thus creating a trade-off in this system, such that a lower degree of oil supersaturation is used to favor high polymer supersaturation and thus faster capsule stabilization rates. The degree of supersaturation experienced by the oil is shown to be the greatest at the lowest flow rate tested (14.2 mL/h), in comparison to the highest flow rate tested (142 mL/h) at which the degree of supersaturation is the smallest, while the inverse is true of polymer supersaturation. These results suggest that the oil nucleation rate is greater under low-flow conditions (total flow rate ≤20 mL/h), and thus, a greater degree of nucleus formation and aggregation occurs prior to stabilization by co-precipitating the polymer, which only will occur further downstream once the acetone mass fraction crosses the polymer cloud point. Also, a previous work⁵ has shown that for dextran 40 kDa with a broad molecular weight distribution, complete polymer precipitation does not occur until an acetone mass fraction of about 0.45, further compounding the coprecipitation trade-off. To generalize this concept, Figure 5b,c shows that the coprecipitation trade-off holds true for the range of conditions studied here; conditions

favoring higher oil supersaturation also favor lower polymer supersaturation (or unsaturated conditions) and that the stabilization and thus final diameter of the capsules are controlled by the polymer supersaturation state, reliably predicting the trend. Plotting the total flow rate as a function of the oil or polymer degree of supersaturation shows that these two are coupled (Figure S3), which could be overcome by use of a micromixer enabling rapid mixing at all flow rates. A benefit of requiring higher polymer supersaturation for capsule stabilization is that such conditions occur at high flow rates above 100 mL/h, aligning with fast mixing timescales creating more uniform precipitation conditions as seen in Figure 4a. Our work thus provides a robust and continuous method of controlling the degree of oil and polymer supersaturation in the steady state by varying the flow and/ or geometry conditions using a co-axial microfluidic device, enabling the study of coprecipitation conditions both experimentally and computationally.

We finally test the generality of our finding by fabricating nanocapsules using the ternary system of hexadecane/acetone/ water which has a distinct phase diagram from that of Miglyol/ acetone/water,5,6 with coprecipitated dextran. A scheme like that of Figure 2a is undertaken, in which device geometry is held constant, and the total flow rate is varied across an order of magnitude. The average capsule diameter changes from about 145 to 90 nm across the range of flow rates tested as shown in Figure 6a. Representative STEM micrographs and corresponding size histograms of the hexadecane capsules are shown in Figure S5. Interestingly, despite similar flow rates and identical geometries, the average diameters of the formed capsules appear to differ significantly, although there is an extent of error bar overlap. To verify that the in situ oil and polymer degrees of supersaturation for this system follow the same trend as was shown for the Miglyol ternary system, CFD simulations are used to simulate the mixing environment, and the results in terms of position on the phase diagram are shown in Figure S4. Again, we observe that larger degrees of oil supersaturation in the mixing zone trade off with smaller

degrees of polymer supersaturation, consistent with what we observed in the Miglyol case. The similarity between the Miglyol and hexadecane systems is seen best when comparing capsule diameters against polymer supersaturation as shown in Figure 6b, where a greater degree of alignment is seen between the two systems, thus confirming our original observation that this coprecipitation scheme is driven by the polymer supersaturation and interfacial stabilization.

CONCLUSIONS

In conclusion, this work has shown the ability to control the average diameters of oil core/polymer shell nanocapsules that are co-precipitated in glass capillary microfluidics via control of the total flow rate and the inner capillary taper diameter, which affects the degree of supersaturation that the oil and polymer experience during nanoprecipitation. Microfluidics enables the study of the degrees of oil and polymer supersaturation for a precisely reproducible controlled condition. This understanding of local supersaturation degrees is discussed quantitatively based on ternary phase diagrams comprising the oil, polymer, solvent, and nonsolvent. The link between experimental conditions and phase diagram location is established via CFD simulations of the conditions tested. There is a trade-off between high degrees of oil supersaturation, desirable for rapid oil nucleation followed by halting further nucleation, occurring concurrently with low degrees of polymer coprecipitation that drives its precipitation and interfacial stabilization. Additionally, if the oil precipitation conditions occur below the polymer cloud point, co-precipitation is not observed, and the droplets are stabilized further downstream, resulting in larger nanocapsules. By combining microfluidic technology and CFD with Ouzo phase diagrams, we present a systematic approach to controlling the size of nanocapsules. Future work includes understanding the effects of flow conditions on the core/shell size ratio, using a polymer that starts in the organic phase alongside the oil and precipitates via water as its nonsolvent which should remove the oil/polymer supersaturation tradeoff, use of a micromixer device to decouple mixing speeds and degrees of both oil and polymer supersaturation, and studying the number density of nanocapsules produced under different conditions.

ASSOCIATED CONTENT

Supporting Information

The Supporting Information is available free of charge at https://pubs.acs.org/doi/10.1021/acs.langmuir.3c00183.

Picture of an actual microfluidic device used for experiments in this study; details of the inner capillary diameter, total flow rate, resulting nanocapsule diameter, and coefficient of variation for the range of conditions illustrated; effect of the flow rate ratio on the average capsule size; relationship between the total flow rate and oil/polymer supersaturation; ternary phase diagram interpretation for understanding the size variation of hexadecane—dextran nanocapsules; and representative STEM micrographs and size histograms of hexadecane/dextran capsules (PDF)

AUTHOR INFORMATION

Corresponding Author

Daeyeon Lee – Department of Chemical and Biomolecular Engineering, University of Pennsylvania, Philadelphia, Pennsylvania 19104, United States; o orcid.org/0000-0001-6679-290X; Email: daeyeon@seas.upenn.edu

Authors

Joseph Rosenfeld – Department of Chemical and Biomolecular Engineering, University of Pennsylvania, Philadelphia, Pennsylvania 19104, United States

Francois Ganachaud — Complex Assemblies of Soft Matter, UMI 3254, Solvay/CNRS/UPenn, Bristol, Pennsylvania 19007, United States; Université de Lyon, CNRS, Université Claude Bernard Lyon 1, INSA-Lyon, Université Jean Monnet, UMR5223, Ingénierie des Matériaux Polymères, F69621 Villeurbanne Cedex, France; Occid.org/0000-0003-2658-2734

Complete contact information is available at: https://pubs.acs.org/10.1021/acs.langmuir.3c00183

Author Contributions

The manuscript was written through contributions of all authors. All authors have given approval to the final version of the manuscript.

Funding

This work was partially supported by NSF-2110611. J.R. was also supported by the Ralph Landau Fellowship Fund at Penn Engineering.

Notes

The authors declare the following competing financial interest(s): Daeyeon Lee is the co-founder of InfiniFluidics.

ABBREVIATIONS

CFD, computational fluid dynamics; IPDI, isophorone diisocyanate; DLS, dynamic light scattering; STEM, scanning transmission electronic microscopy

REFERENCES

- (1) Couvreur, P.; Barratt, G.; Fattal, E.; Vauthier, C. Nanocapsule technology: a review. *Crit. Rev. Ther. Drug Carrier Syst.* **2002**, *19*, 99–124
- (2) Rosset, V.; Ahmed, N.; Zaanoun, I.; Stella, B.; Fessi, H.; Elaissari, A. Elaboration of argan oil nanocapsules containing naproxen for cosmetic and transdermal local application. *J. Colloid Sci. Biotechnol.* **2012**, *1*, 218–224.
- (3) Barreras-Urbina, C. G.; Ramírez-Wong, B.; López-Ahumada, G. A.; Burruel-Ibarra, S. E.; Martínez-Cruz, O.; Tapia-Hernández, J. A.; Rodriguez Felix, F. Nano-and micro-particles by nanoprecipitation: Possible application in the food and agricultural industries. *Int. J. Food Prop.* **2016**, *19*, 1912–1923.
- (4) Mora-Huertas, C. E.; Fessi, H.; Elaissari, A. Polymer-based nanocapsules for drug delivery. *Int. J. Pharm.* **2010**, 385, 113–142.
- (5) Yan, X.; Ramos, R. A. N. S.; Alcouffe, P.; Munoz, L. E.; Bilyy, R. O.; Ganachaud, F.; Bernard, J. Programmable hierarchical construction of mixed/multilayered polysaccharide nanocapsules through simultaneous/sequential nanoprecipitation steps. *Biomacromolecules* **2019**, *20*, 3915–3923.
- (6) Yan, X.; Delgado, M.; Fu, A.; Alcouffe, P.; Gouin, S. G.; Fleury, E.; Katz, J. L.; Ganachaud, F.; Bernard, J. Simple but precise engineering of functional nanocapsules through nanoprecipitation. *Angew. Chem., Int. Ed.* **2014**, *53*, 6910–6913.
- (7) Yan, X.; Bernard, J.; Ganachaud, F. Nanoprecipitation as a simple and straightforward process to create complex polymeric colloidal morphologies. *Adv. Colloid Interface Sci.* **2021**, 294, 102474.
- (8) Yan, X.; Alcouffe, P.; Sudre, G.; David, L.; Bernard, J.; Ganachaud, F. Modular construction of single-component polymer nanocapsules through a one-step surfactant-free microemulsion templated synthesis. *Chem. Commun.* **2017**, *53*, 1401–1404.

- (9) Iglicki, D.; Goubault, C.; Nour Mahamoud, M.; Chevance, S.; Gauffre, F. Shedding Light on the Formation and Stability of Mesostructures in Ternary "Ouzo" Mixtures. *J. Colloid Interface Sci.* **2023**, *633*, 72–81.
- (10) Vitale, S. A.; Katz, J. L. Liquid droplet dispersions formed by homogeneous liquid—liquid nucleation: "The Ouzo effect". *Langmuir* **2003**, *19*, 4105–4110.
- (11) Ganachaud, F.; Katz, J. L. Nanoparticles and nanocapsules created using the Ouzo effect: spontaneous emulsification as an alternative to ultrasonic and high-shear devices. *ChemPhysChem* **2005**, 6, 209–216.
- (12) Wu, B.; Yang, C.; Li, B.; Feng, L.; Hai, M.; Zhao, C. X.; Chen, D.; Liu, K.; Weitz, D. A. Active encapsulation in biocompatible nanocapsules. *Small* **2020**, *16*, 2002716.
- (13) Fessi, H.; Puisieux, F.; Devissaguet, J. P.; Ammoury, N.; Benita, S. Nanocapsule formation by interfacial polymer deposition following solvent displacement. *Int. J. Pharm.* **1989**, *55*, R1–R4.
- (14) Saad, W. S.; Prud'homme, R. K. Principles of nanoparticle formation by flash nanoprecipitation. *Nano Today* **2016**, *11*, 212–227.
- (15) Mockus, L.; Peterson, J. J.; Lainez, J. M.; Reklaitis, G. V. Batchto-batch variation: a key component for modeling chemical manufacturing processes. *Org. Process Res. Dev.* **2015**, *19*, 908–914.
- (16) Anderson, N. G. Practical use of continuous processing in developing and scaling up laboratory processes. *Org. Process Res. Dev.* **2001**, *5*, 613–621.
- (17) Wu, J.; Yadavali, S.; Issadore, D. A.; Lee, D. Ultrahigh Throughput On-Chip Synthesis of Microgels with Tunable Mechanical Properties. *Adv. Mater. Technol.* **2022**, *7*, 2101160.
- (18) Wu, J.; Yadavali, S.; Lee, D.; Issadore, D. A. Scaling up the throughput of microfluidic droplet-based materials synthesis: A review of recent progress and outlook. *Appl. Phys. Rev.* **2021**, *8*, 031304.
- (19) Yadavali, S.; Lee, D.; Issadore, D. Robust microfabrication of highly parallelized three-dimensional microfluidics on silicon. *Sci. Rep.* **2019**, *9*, 12213.
- (20) Yadavali, S.; Jeong, H. H.; Lee, D.; Issadore, D. Silicon and glass very large scale microfluidic droplet integration for terascale generation of polymer microparticles. *Nat. Commun.* **2018**, *9*, 1222.
- (21) Ding, S.; Anton, N.; Vandamme, T. F.; Serra, C. A. Microfluidic nanoprecipitation systems for preparing pure drug or polymeric drug loaded nanoparticles: an overview. *Expert Opin. Drug Delivery* **2016**, 13, 1447–1460.
- (22) Tao, J.; Chow, S. F.; Zheng, Y. Application of flash nanoprecipitation to fabricate poorly water-soluble drug nanoparticles. *Acta Pharm. Sin. B* **2019**, *9*, 4–18.
- (23) Martins, J. P.; Torrieri, G.; Santos, H. A. The importance of microfluidics for the preparation of nanoparticles as advanced drug delivery systems. *Expert Opin. Drug Delivery* **2018**, *15*, 469–479.
- (24) Xu, Y.; Hu, B.; Xu, J.; Wu, J.; Ye, B. Preparation of biodegradable polymeric nanocapsules for treatment of malignant tumor using coaxial capillary microfluidic device. *Cancer Biother.Radiopharm.* 2020, 35, 570–580.
- (25) Hajian, R.; Hardt, S. Formation and lateral migration of nanodroplets via solvent shifting in a microfluidic device. *Microfluid. Nanofluid.* **2015**, *19*, 1281–1296.
- (26) Liu, D.; Zhang, H.; Cito, S.; Fan, J.; Mäkilä, E.; Salonen, J.; Hirvonen, J.; Sikanen, T. M.; Weitz, D. A.; Santos, H. A. Core/shell nanocomposites produced by superfast sequential microfluidic nanoprecipitation. *Nano Lett.* **2017**, *17*, 606–614.
- (27) Haase, M. F.; Stebe, K. J.; Lee, D. Continuous fabrication of hierarchical and asymmetric bijel microparticles, fibers, and membranes by solvent transfer-induced phase separation (STRIPS). *Adv. Mater.* **2015**, *27*, 7065–7071.
- (28) Shah, R. K.; Shum, H. C.; Rowat, A. C.; Lee, D.; Agresti, J. J.; Utada, A. S.; Chu, L. Y.; Kim, J. W.; Fernandez-Nieves, A.; Martinez, C. J.; Weitz, D. A. Designer emulsions using microfluidics. *Mater. Today.* 2008, 11, 18–27.

- (29) Xia, H. M.; Wang, Z. P.; Koh, Y. X.; May, K. T. A microfluidic mixer with self-excited 'turbulent' fluid motion for wide viscosity ratio applications. *Lab Chip* **2010**, *10*, 1712–1716.
- (30) Fang, R. H.; Chen, K. N. H.; Aryal, S.; Hu, C. M. J.; Zhang, K.; Zhang, L. Large-scale synthesis of lipid—polymer hybrid nanoparticles using a multi-inlet vortex reactor. *Langmuir* **2012**, *28*, 13824—13829.
- (31) Anton, N.; Bally, F.; Serra, C. A.; Ali, A.; Arntz, Y.; Mely, Y.; Zhao, M.; Marchioni, E.; Jakhmola, A.; Vandamme, T. F. A new microfluidic setup for precise control of the polymer nanoprecipitation process and lipophilic drug encapsulation. *Soft Matter* **2012**, *8*, 10628–10635.
- (32) Yan, X.; Sivignon, A.; Alcouffe, P.; Burdin, B.; Favre-Bonté, S.; Bilyy, R.; Barnich, N.; Fleury, E.; Ganachaud, F.; Bernard, J. Brilliant glyconanocapsules for trapping of bacteria. *Chem. Commun.* **2015**, *51*, 13193–13196.
- (33) Lebouille, J. G.; Stepanyan, R.; Slot, J. J.; Cohen Stuart, M.; Tuinier, R. Nanoprecipitation of polymers in a bad solvent. *Colloids Surf., A* **2014**, *460*, 225–235.

☐ Recommended by ACS

New Lyotropic Complex Fluid Structured in Sheets of Ellipsoidal Micelles Solubilizing Fragrance Oils

Vera Tchakalova, Antonio Martins Figueiredo Neto, et al.

JULY 31, 2023 ACS OMEGA

READ 🗹

Controllable Monodisperse Amphiphilic Janus Microparticles

Quan-Wei Cai, Liang-Yin Chu, et al.

JUNE 21, 2023

ACS APPLIED POLYMER MATERIALS

READ 🗹

Spontaneous Formation Mechanisms of Droplets in Step Emulsification

Taoxian Zhang, Liang-Yin Chu, et al.

MAY 08, 2023

INDUSTRIAL & ENGINEERING CHEMISTRY RESEARCH

READ 🗹

Aqueous Bubbles Stabilized with Millimeter-Sized Polymer Plates

Yuri Sakurai, Syuji Fujii, et al.

FEBRUARY 28, 2023

LANGMUIR

READ **C**

Get More Suggestions >